Piezoelectric MEMS for vibrations sensing

Author: Marco Locorotondo

Internship supervisor: Prof. Guillermo Villanueva
Internship supervisor: Daniel Moreno García
Academic supervisor: Prof. Maria Luisa Della Rocca
Academic supervisor: Prof. Carlo Ricciardi

Politecnico di Torino
Université Paris Cité
École Polytechnique Fédérale de Lausanne

Master's thesis project
Advanced NEMS laboratory - EPFL

Nanotechnologies and Quantum devices (NANOQUAD)
2022/2023

Abstract

Vibration sensors, also known as vibrometers, are essential components for maintaining the safety and reliability of various machines, such as aircraft engines. Vibrometers are capable of detecting very small vibrations, which can be caused by acceleration or pressure variations in the environment. However, the strict requirements for safety, resolution, endurance, and lifetime in the aerospace industry have caused the technology to evolve slowly.

Indeed in this sector sensors have to work in harsh environments and at the same time high performances are required. MEMS-technologies based accelerometers were introduce to fulfill these requirements by substituting the old bulk technology: they are smaller, more responsive, more robust.

In particular the current piezoelectric devices implemented for aerospace applications consist in boxes that contain a proof mass positioned on top of the piezoelectric material. This last one will be deformed due to the motion of the mass when the sensor is subjected to an acceleration.

Therefore, the objective of this research project is to investigate the potential of piezoelectric MEMS-based accelerometers as the next generation vibrometers. This work begins with a characterization of previous vibrometers to identify their strengths and limitations. Subsequently, the research focuses on the simulation, design, and fabrication of new devices that could potentially offer improved performance and greater reliability.

Acknowledgments

I am deeply grateful to Prof. Guillermo Villanueva for his unwavering belief in my abilities and consistent motivation during the challenging phases of this thesis. Moreover, his professional guidance and personal mentorship have played a crucial role in shaping my academic journey, making this learning experience both profound and enjoyable.

I would like to express my utmost appreciation to Daniel Moreno Garcìa, whose expert guidance, infinite patience, and continuous support throughout this research endeavor have been priceless. His profound knowledge and insightful perspectives have consistently enlightened me, dispelling any doubts and directing me towards the right path. Without his unwavering assistance, this thesis would have taken a completely different form.

I also extend my heartfelt gratitude to the entire ANEMS group, particularly Damien Maillard, Kevin Uning, and Marco Liffredo, for their invaluable assistance in the process flow and fabrication technical aspects. Their extensive expertise in cleanroom processes has been immensely helpful.

Contents

List of Figures

Chapter 1

Introduction

This project aims to develop a vibrometer for the aerospace company Meggitt within the ANEMS laboratory. The Advanced NEMS group aims to go beyond the current State-of-the-Art in NEMS and MEMS on two particular fields: sensing and communications. This is done by taking a holistic approach, where everything is addressed from the design until the final application, going through simulation, fabrication and characterization.

The wanted vibrometer is a uniaxial accelerometer specifically designed for aerospace applications. It will be utilized within the gearbox of an aircraft to continuously measure vibration (Fig.1.1, Fig.1.2). The device functions as an acceleration sensor and plays a crucial role when the frequency surpasses a certain threshold, in such case the aircraft's computer system will alert technicians about the need for maintenance.
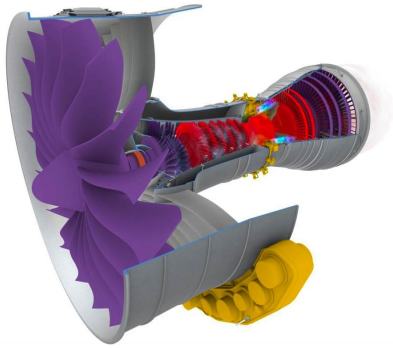
Figure 1.1: Aircraft engine ([1])
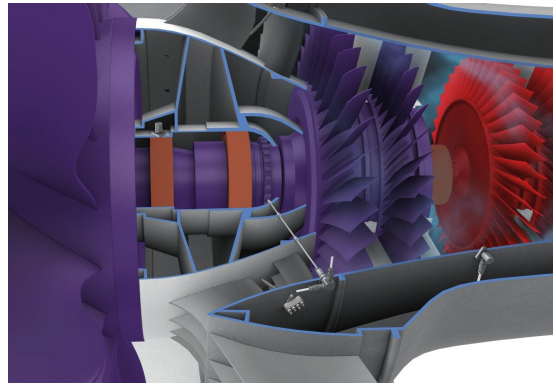
Figure 1.2: Gearbox that presents on the external shell vibration sensors([1])

The initial stages of this project were undertaken as part of a previous master's thesis [6]. The initial work involved designing, fabricating, and conducting theoretical calculations and simulations. Subsequently, another master's thesis student [5] continued the project by utilizing the previous findings to fabricate a large quantity of devices.

The ongoing pursuit entails extending the preceding work through the conduction of additional simulations aimed at optimizing performance and resolving any lingering concerns. Furthermore, upon the finalization of an improved design, the next step will be the fabrication of the new devices.

1.1 Accelerometer

An accelerometer is a device that measures the acceleration of an object or the rate of change of its velocity. It is typically used to measure linear acceleration, but depending on the design it can also measure rotational acceleration, as in the case of a angular rate sensor. Accelerometers can be used in a wide range of applications, from detecting seismic activity to monitoring the movement of vehicles and measuring vibration in machinery.

The basics structure of an accelerometer is composed by an inertial mass and a spring. When the accelerometer is subjected to acceleration, the inertial mass moves in response to the force, causing a displacement or strain in the suspension element.
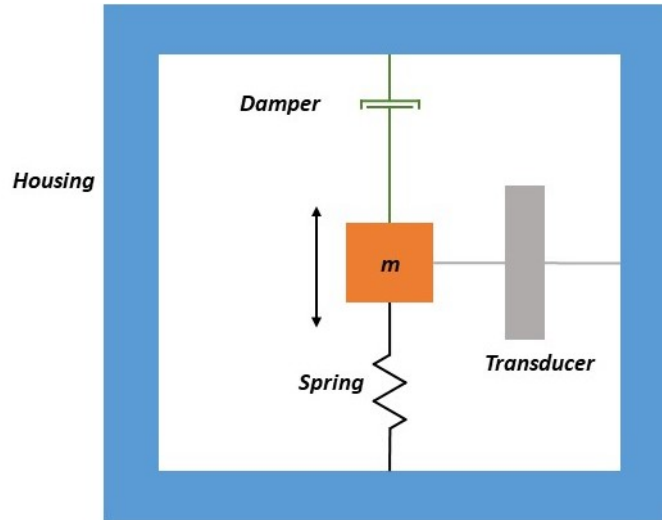
Figure 1.3: Representation of a usual bulk accelerometer

In order to measure the acceleration the mechanical motion has to be converted into an electrical signal that can be processed and analyzed. This aim is achieved through the a specific transduction mechanism. This last one is based on the conversion of a type of energy to another for the purpose of measurement or information transfer.

In the next section, it is provided an overview on the MEMS technology highlighting its importance in the evolution of sensors and particularly accelerometers.

1.1.1 MEMS technology

MEMS (Microelectromechanical Systems) technology offers significant advantages over bulk technology when it comes to sensors, actuators, and particularly accelerometers.

Firstly, MEMS devices are miniaturized and lightweight, allowing for integration into small-scale systems and portable devices without compromising functionality. This compact size enables widespread deployment in various applications, including consumer electronics, automotive safety systems, and medical devices.

Moreover, this technology offers improved reliability and durability due to its monolithic construction, with sensors and associated electronics fabricated on a single chip. This eliminates the need for external connections and reduces the risk of failure due to mechanical stress or environmental factors. Overall, the numerous benefits of MEMS technology, such as miniaturization, high precision, low cost, low power consumption and enhanced reliability, make it a superior choice for accelerometers and other sensing and actuating applications, propelling advancements in various industries.

MEMS accelerometers offer high precision and sensitivity, making them ideal for measuring even the smallest changes in acceleration. Their small form factor also allows for the placement of multiple accelerometers in a single device, enabling multi-axis sensing for more accurate measurements. Furthermore, this technology allows the access to harsh environments in which extreme levels of temperature, radiation, acceleration and pressure are reached. Indeed, MEMS have demonstrated robustness to high-g shock and high temperature. For this reason they are well suited for aerospace industry, according to the purpose of this project [2].

1.2 Accelerometer parameters

In order to fully describe an accelerometer we need to evaluate the following parameters([7, 8]):

- Sensitivity: the ratio of the change in output signal to the change in acceleration, usually expressed in volts per g (acceleration due to gravity);

- Dynamic range: the range of values between the minimum and the maximum detectable acceleration of the accelerometer;

- Resolution: the smallest detectable change in acceleration that an accelerometer can measure;

- Bandwidth: the range of frequencies over which an accelerometer can measure acceleration with a specified degree of accuracy;

- Linearity: The degree to which the output of an accelerometer is proportional to the input acceleration over its full range;

- Bias: The output voltage of an accelerometer when it is not subjected to any acceleration. Bias can be caused by various factors, such as temperature changes, gravitational forces, or mechanical stresses;

- Noise: The random variation in the output voltage of an accelerometer when it is not subjected to any acceleration;

- Temperature sensitivity: The degree to which the output of an accelerometer is affected by changes in temperature.

All these definitions are useful for understanding the following chapters.

Chapter 2

Piezoelectricity

The piezoelectric effect manifests as a linear relationship between mechanical and electrical quantities [7]. The application of a mechanical load on a piezoelectric material induces a mechanical deformation, leading to a significant alteration in the electric polarization at a macroscopic level. When appropriately covered with electrodes, this material allows for the measurement of electric voltages or charges directly associated with the mechanical deformation. Specifically, the conversion of mechanical energy to electrical energy is known as the *direct piezoelectric effect*, whereas the *inverse piezoelectric effect* describes the conversion from electrical to mechanical energy. Since both effects require changes of electric polarization, piezoelectric materials do not contain any free electric charges and, thus, these materials are electrical insulators. To understand the piezoelectric effect, we can consider a quartz crystal (SiO_2) as the piezoelectric material, which is covered with electrodes on its top and bottom surfaces. Initially, in its pristine state, the center C_{Q+} of positive charges (silicon ions) geometrically coincides with the center C_{Q-} of negative charges (oxygen ions), as showed in the figures on the left (Fig.2.1). Consequently, the material is electrically neutral.
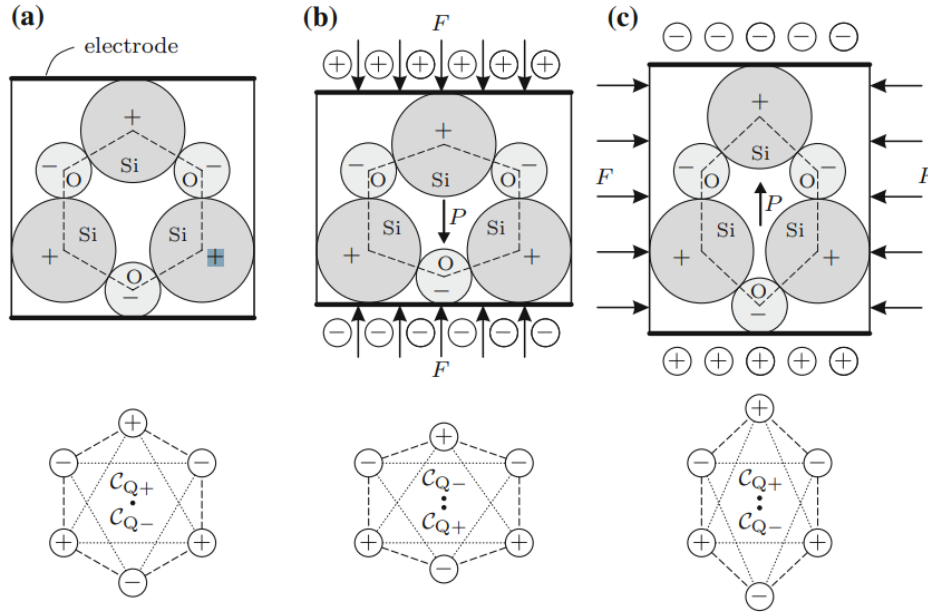

Figure 2.1: Simplified inner structure of quartz crystal SiO_2 covered with electrodes at top and bottom surface; **a** no mechanical load, original state; **b** longitudinal and **c** transverse mode of direct piezoelectric effect due to mechanical forces

However, when a mechanical load is applied, the material undergoes deformation, causing the centers of charges to deviate from their original positions. This discrepancy gives rise to electric dipole moments that originate from C_{Q-} and point towards C_{Q+}. The electric polarization $\mathbf{P}$ characterizes this dipole moment. The magnitude $||\mathbf{P}||_2$ of the electric polarization increases with a larger geometric separation between C_{Q-} and C_{Q+}. In order to neutralize the electric polarization within the material, which causes an electrical imbalance, charges are induced on the electrodes. When the electrodes are short-circuited, a flow of charge occurs. Moreover, by considering the orientations of the mechanical load and the resulting electric polarization, we can identify various modes of piezoelectricity. For example, in the fig. 2.1b and fig. 2.1c respectively longitudinal and transverse mode are showed.

In the case of the inverse piezoelectric effect, the same phenomena occur within the piezoelectric material, but in the opposite direction.

Let us now provide the constitutive equations of the piezoelectric form, particularly focusing on the strain-charge relationship. In this context, the following equations describe the direct and inverse effects:

$$D_m = \epsilon_{mn}^T E_n + d_{mkl} T_{kl} \tag{2.1}$$

$$S_{ij} = d_{ijn} E_n + s_{ijkl}^E T_{kl} \tag{2.2}$$

Here, D_m represents the electrical displacement, E_n denotes the electrical field, T_{kl} represents the mechanical stress, S_{ij} signifies the mechanical strain, ϵ_{mn}^T denotes the electric permittivity for constant mechanical stress (indicated by the superscript T), s_{ijkl}^E is the elastic compliance constant for constant electric field intensity, and d_{mkl} represents the piezoelectric strain constant.

For completeness it is important to mention that there is also the stress-charge form for the constitutive equations:

$$D_m = \epsilon_{mn}^S E_n + e_{mkl} S_{kl} \tag{2.3}$$

$$T_{ij} = -e_{ijn} E_n + c_{ijkl}^E S_{kl} \tag{2.4}$$

with the elastic stiffness constants c_{ijkl}^E for constant dielectric field intensity and the piezoelectric stress constants e_{mkl}. In particular direct piezoelectric effect is described by both eq.(2.1) and eq.(2.3), whereas eq.(2.2) and eq.(2.4) account for the inverse effect.

Taking into account the symmetries within the tensors of rank four for the mechanical field (s_{ijkl}, c_{ijkl}) as well as within the tensors of rank three for piezoelectric coupling (d_{mkl}, e_{mkl}), we are able to transform the tensor equations to matrix equations, following the Voigt notation we obtain for the strain-charge form:

$$\mathbf{D} = [\epsilon^T]\mathbf{E} + [\mathbf{d}]\mathbf{T} \tag{2.5}$$

$$\mathbf{S} = [\mathbf{d}]^t\mathbf{E} + [\mathbf{s}^E]\mathbf{T} \tag{2.6}$$

The vectors $\mathbf{D}$ and $\mathbf{E}$ have three components each, while the vectors $\mathbf{T}$ and $\mathbf{S}$ have six components each. Moreover, the reduced tensors describing mechanical properties ($[\mathbf{s}],[\mathbf{c}]$) and piezoelectric coupling $[\mathbf{d}]$ exhibit the dimensions 6x6 and 3x6 respectively. On the contrary, the tensor for electrical properties $[\epsilon]$ is of dimension 3x3. All of this information is valuable for gaining a better understanding of how to establish the simulation discussed in the next chapters.

2.1 Electromechanical coupling factor

The electromechanical coupling coefficient is a significant parameter for evaluating piezoelectric materials. Various definitions of this coefficient exist, each with its unique characteristics. This figure of merit concerns the conversion of mechanical into electrical energy as well as of electrical into mechanical energy, which are here given by ($1 \leq i \leq 3; 1 \leq p \leq 6$):

$$Mechanical\ energy\ per\ unit\ volume: W_{mech} = \frac{S_p T_p}{2} \tag{2.7}$$

$$Electrical\ energy\ per\ unit\ volume: W_{elec} = \frac{D_i T_i}{2} \tag{2.8}$$

Furthermore, by definition the electromechanical coupling coefficient k^2 in the case of direct piezoelectric effect is the ratio between the mechanical energy converted into electrical energy and the mechanical input energy. In particular taking into account the article [9], they utilize the expression:

$$k_{33}^2 = \frac{d_{33}^2}{\epsilon_{33}^T \cdot S_{33}^E} \tag{2.9}$$

The conversion of mechanical energy into electrical energy and vice versa is inherently incomplete. As a result, both k^2 and k are always less than 1.

2.2 Modes of the piezoelectric effect

The constitutive equations for piezoelectricity outline 18 possibilities (d_{11},..., d_{36}) for coupling electrical and mechanical fields within piezoelectric materials, which are divided into four modes: longitudinal, transverse, longitudinal shear, and transverse shear. These modes determine how mechanical inputs are converted into electrical outputs. For the direct piezoelectric effect, where mechanical stress results in an electric flux density and a change in electric polarization, the modes can be described as follows:

- **Longitudinal mode (L)**: Includes d_{11}, d_{22}, and d_{33}. A normal stress applied in one direction leads to a change in electric polarization in the same direction.

- **Transverse mode (T)**: Includes d_{12}, d_{13}, d_{21}, d_{23}, d_{31}, and d_{32}. Unlike the longitudinal mode, the change in electric polarization occurs perpendicular to the applied mechanical load.

- **Longitudinal shear mode (SL)**: Includes d_{14}, d_{25}, and d_{36}. When a shear stress is applied, the polarization changes perpendicular to the sheared plane of the material.

- **Transverse shear mode (ST)**: Includes d_{15}, d_{16}, d_{24}, d_{26}, d_{34}, and d_{35}. In contrast to the longitudinal shear mode, the electric polarization changes within the plane of the sheared material.

These modes apply not only to the direct piezoelectric effect but also to the inverse piezoelectric effect and all other forms of constitutive equations for piezoelectricity. Figure 2.2 provides a visual representation of these modes using a cubical-shaped piezoelectric material.
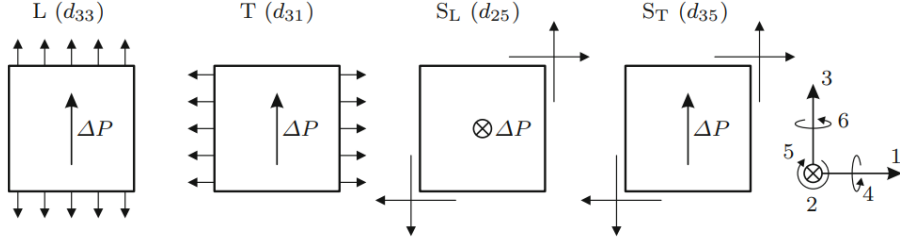
Figure 2.2: Examples for longitudinal (L), transverse (T), longitudinal shear (SL), and transverse shear modes (ST) of piezoelectricity within cubical-shaped piezoelectric material; macroscopic change ΔP of electric polarization.

2.3 Piezoelectric accelerometers

The decision of developing piezoelectric accelerometer was made by the first master's thesis student after an extensive review of relevant literature. Specifically, Elies et al. conducted a comprehensive investigation of various accelerometer types, as documented in their study [4]. Their thorough analysis revealed that piezoelectric accelerometers possess several noteworthy advantages in terms of overload shock limits, measurement range, and operating temperature. Furthermore, these accelerometers demonstrate rapid response, high linearity, and exceptional efficiency. Taking these factors into consideration, it becomes evident that a piezoelectric device with charge readout emerges as the most appropriate and optimal choice for the present project.

After that it was important also to choose the mode of the accelerometer and the appropriate piezoelectric material. Therefore various accelerometer designs have been investigated in the literature.

Three common operating modes for piezoelectric accelerometers with charge output are widely used: bending mode (d_{31}), compression mode (d_{33}), and shear mode (d_{15}). These modes correspond to specific piezoelectric strain constants that determine the amount of charge generated per applied force [3].

The bending mode involves inducing an electric field in direction 3 when the material experiences stress along direction 1. The compression mode aligns the stress direction with the generated electric field (direction 3) using the d_{33} piezoelectric constant. The shear mode utilizes the d_{15} piezoelectric constant, where shear stress is applied in the σ_{31} direction while the material is polarized in direction 1, with charge extraction perpendicular to both stress and polarization directions.

After analysing all the advantages and disadvantages of each accelerometer design, in the previous work [6] it was decided that the bending mode has favorable characteristics with the best sensitivity-to-mass ratio and simpler fabrication process.

Based on existing literature, the commonly adopted bending mode designs for piezoelectric accelerometers are circular and square membranes featuring a central mass. While these designs resemble cantilevers with proof masses, they are essentially rotations around the end mass of the cantilever. The preference for these designs arises from their utilization of fully clamped membranes, which enhances stability, and their symmetrical configuration that maximizes fill factors. Consequently, these designs exhibit higher charge generation and improved robustness. Notably, Yaghootkar et al. observed significantly elevated cross-axis sensitivity in square piezoelectric accelerometers, favoring the selection of circular designs for uniaxial piezoelectric accelerometers [10, 11].

Therefore circular membranes emerge as the most optimal choice due to their maximized fill factor,

robustness, and low cross-axis sensitivity. Considering these design criteria, the subsequent step involved assessing the design tradeoffs to optimize the geometric parameters of a uniaxial circular piezoelectric accelerometer with charge output.

2.3.1 Materials

The materials under consideration for the accelerometer project are AlN and PZT, both of which are accessible in EPFL's CMi cleanroom. In the bending mode design, the d_{31} component of the piezoelectric materials will be employed. This choice stems from the fact that polarization is induced along the z-axis when a stress is applied along the x-axis. The piezoelectric strain constants for these materials are listed below:

PZE material	d_{31} [C/N]
AlN	-1.92×10^{-12}
PZT-4	-1.23×10^{-10}
PZT-5H	-2.74×10^{-10}

Table 2.1: Piezoelectric materials available in EPFL's CMi cleanroom and their respective piezoelectric strain constants d_{31}.

While PZT appears to generate more charge per applied force, it is crucial to examine the Curie temperature of these materials. The Curie temperature denotes the transition temperature at which materials lose their permanent magnetic properties [4]. Typically, piezoelectric materials with superior charge generation exhibit lower Curie temperatures. The table below displays the Curie temperatures for the considered materials.
Moreover PZT contains a large amount of lead. It is highly contaminant and belongs to hazardous substances ([7]). Indeed it is strongly discouraged the deposition of lead within the EPFL's cleanroom. Given the preference for a higher Curie temperature in harsh environments and the aforementioned issues, AlN has been selected as the piezoelectric material for this particular application.

PZE material	Curie temperature [°C]
AlN	Theoretical: 700; Oxidized test: 600
PZT-4	325
PZT-5H	195

Table 2.2: Piezoelectric materials available in EPFL's CMi cleanroom and their respective Curie temperatures.

2.3.2 Operating Space

The fundamental design considerations for a piezoelectric accelerometer encompass the dynamic range and bandwidth, both of which play crucial roles in its performance. The dynamic range is contingent upon two primary factors: the maximum detectable acceleration, governed by the charge generation linearity, and the minimum detectable acceleration, influenced by the charge amplifier characteristics.
On the other hand, the bandwidth of the accelerometer hinges on several aspects, including the

resonance frequency, quality factor, and thermomechanical noise[1]. The resonance frequency and quality factor collectively establish the upper limit for the frequency response, while the thermomechanical noise governs the lower limit. Consequently, with knowledge of these parameters, the overall bandwidth can be determined.

These parameters and their relationships can be summarized and presented in a graph, as shown below.
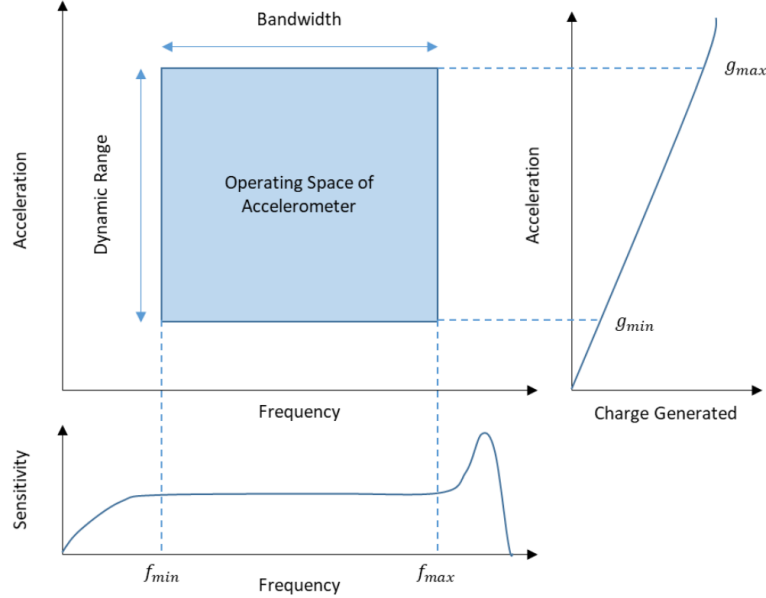

Figure 2.3: Relationship between accelerometer parameters. [6]

The resonant frequency of any structure can be easily described by the standard equation:

$$f = \frac{1}{2\pi}\sqrt{\frac{k}{m}} \tag{2.10}$$

where f is the resonance frequency of the structure, k is the stiffness of the structure, and m is the mass.

For a standard piezoelectric accelerometer, the sensitivity is described by the displacement per acceleration, hence the equation:

$$S_x = \frac{x}{a} = \frac{m}{k} \tag{2.11}$$

where S_x is the mechanical sensitivity, x is the displacement, and a is the acceleration. Therefore, we find the relationship between mechanical sensitivity and the resonant frequency to be:

$$S_x = \frac{1}{f^2} \tag{2.12}$$

This relationship leads to a troublesome optimization problem: it is difficult to have a device that operates at high frequencies while achieving high sensitivities.

---

[1]Thermomechanical noise is a form of dissipation that can be see as the coupling between a cavity and a thermal reservoir full of randomly distribuited phonons.

Chapter 3

Previous Work

3.1   Theoretical work

The theoretical work conducted in this Master's thesis projects ([6, 5]) aimed to comprehensively understand the fundamental principles and design considerations of piezoelectric sensors in order to achieve higher sensitivities. The chosen piezoelectric material for analysis was aluminum nitride (AlN), considering its lower d_{31} coefficient compared to lead zirconate titanate (PZT). As a result, the z_{offset} parameter was identified as crucial for maximizing sensitivity.

To examine the charge generation in piezoelectric materials, the displacement current equation (I_D) and frequency-dependent displacement field equation ($j\omega$) were derived. These equations considered various factors such as the frequency (ω), input voltage (V_{in}), detection proportionality term (X_n^D), width (w), length (L) and deflection (u_n) of the piezoelectric material.

$$I_D(t) = \int_{A_{elec}} \frac{\partial D(t)}{\partial t} = j\omega \tag{3.1}$$

$$j\omega \in \frac{A_{elec}}{t_{PZE}} V_{in} + j\omega X_n^D \frac{d_{31}}{C_{11}} \frac{wz_{offset}}{L} u_n(\omega) \tag{3.2}$$

In the detection mode, where no input voltage is applied, the generated charge (Q) is proportional to the piezoelectric constant, geometric parameters, deflection, and z_{offset}. The z_{offset} refers to the distance between the piezoelectric material and the neutral axis of the structure. It is important to note that the charge generation (Q) is directly influenced by the deflection (u_n)) and z_{offset}.

The neutral axis, defined as the point within a material where stress is zero, can be calculated using an equation that considers the cross-sectional area (A_i), elastic modulus (E_i)) and position (z_i)) of each layer. In a multi-layer structure, perfect alignment of the piezoelectric material with the neutral axis results in a z_{offset} of zero. Consequently, when an applied force is present, no charge is generated. However, introducing another layer with a non-zero z_{offset} enables the piezoelectric material to generate a charge.

In order to prevent charge cancellation during collection, a configuration with a separated top electrode and a shared ground electrode at the bottom is utilized. This arrangement ensures that the two electrodes are connected in series, optimizing the extraction of charge generated from the bending piezoelectric structure.

In the cited thesis [6] it was highlighted that minimizing the thickness of the piezoelectric layer leads to a larger z_{offset}, which in turn maximizes the charge generation. This observation underscores the importance of reducing the piezoelectric layer thickness to achieve maximum charge extraction.

3.2 Simulation

COMSOL was employed for finite element modeling with the aim of identifying the dimensions that would yield the desired performance characteristics. The following performance targets were considered:

- For low-frequency applications: a resonant frequency of 1 kHz and a charge generation of 1 pC/g.

- For high-frequency applications: a resonant frequency of 100 kHz and a charge generation of 1 fC/g.

Through the analysis, various parameters were investigated, and the corresponding performances are presented in the subsequent table.

Parameters/Performance	Low Frequency Case	High Frequency Case
Membrane Thickness [μm]	14	120
Mass Thickness [μm]	350	350
Membrane Radius [μm]	2000	2000
Electrode Thickness [nm]	50	50
AlN Thickness [nm]	100	100
b/a ratio [unitless]	0.5	0.5
Charge Generation [fC/g]	1068	21.2
Resonant Frequency [kHz]	6.42	115.1
Displacement Sensitivity [m/g]	6.12×10^{-9}	2.2×10^{-11}
Dynamic Range [g]	500	2000
Linearity [%]	3.03	0.01
Cross Axis Sensitivity [%]	< 0.01	< 0.01

Table 3.1: Performance Comparison for Low and High Frequency Cases

The design of a circular piezoelectric accelerometer involved selecting a cost-effective wafer and considering design constraints such as substrate and proof mass thickness, device footprint, and membrane properties. Thicker membranes with larger device radii were found to optimize charge sensitivity. For the final design, a double-sided polished Si wafer with a maximum substrate thickness of 380 μm was chosen, allowing a proof mass thickness of 350 μm to prevent crashing. The device footprint was limited to 5 mm.

3.3 Previous design and fabrication

The final device configuration consists of a squared silicon chip with a membrane and seismic mass formed through a backside etching process. On the front side, two circular electrodes are deposited, comprising a Pt-AlN-Pt sandwich structure. As previously mentioned, the ground (GND) electrode is shared between the inner and external electrodes.
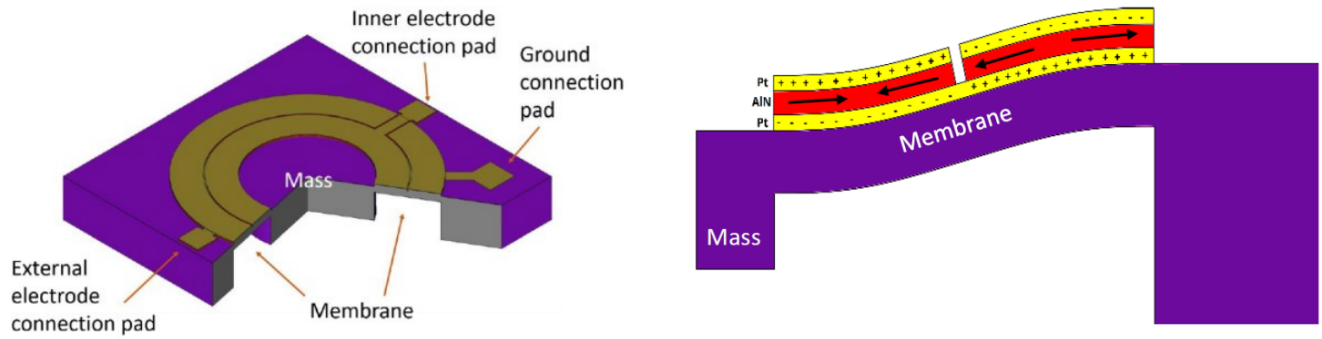
Figure 3.1: Design of the accelerometer

The working principle of this accelerometer involves the following steps:

1. When an acceleration is applied to the device, the mass undergoes movement, causing deformation of the membrane.

2. The deformed membrane constrains the piezoelectric layer, resulting in the generation of electrical charges.

3. These charges accumulate on the electrodes, facilitating the measurement and detection of the applied acceleration.

Several challenges were encountered during the fabrication process ([6]), resulting in the inability to characterize any of the devices produced. The issues include:

- Fences: these are accumulations of the etched Pt that redeposit above the edges of the bottom Pt layer. If they are enough high can create a short circuit between the top and bottom electrodes.

- Over etching of the backside silicon during the release of the membrane, leading to the destruction of some devices.

- Delamination of the top platinum layer: it separated or detached after the etching of the aluminum layer.

These challenges significantly hindered the successful fabrication and characterization of the devices.

In the subsequent fabrication attempt, carried out in a recent master's thesis project ([5]), efforts were made to address the previously mentioned challenges while retaining the same design. Notably, a change was made in the choice of material for the top electrode. Instead of using platinum as in the initial fabrication, molybdenum (Mo) was employed. This alternative material offers comparable conductivity to platinum while being more cost-effective. However, it is important to note that molybdenum is more susceptible to oxidation. Consequently, during the removal of parylene, a protective polymer coating, several devices were found to have experienced oxidation. (Refer to the process flow provided in the appendix A).

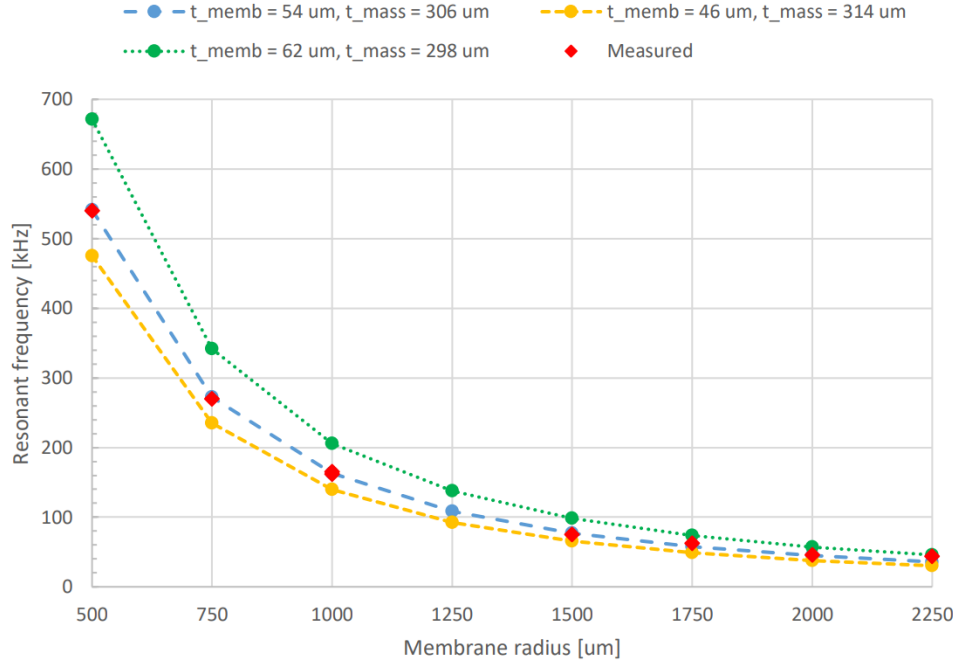## 3.4 First resonance frequency measurements

Figure 3.2: Resonance frequency as a function of membrane radius

The presented graph from the past thesis [5] provides an overview of the resonance frequency measurements conducted on a set of devices derived from a single wafer out of three available options. Specifically, the selected wafer exhibited a membrane thickness of 60 μm. Additionally, the membrane thickness was measured at various points on different chips, yielding an average value of 54 μm with a margin of error of 8 μm. The graph depicts three simulated curves: one representing the resonance frequency based on the average membrane thickness and the other two representing the extreme values considering the aforementioned error. Remarkably, the measured resonance frequencies align precisely with the simulated values, affirming the accuracy of the COMSOL model as a dependable tool for predicting resonance frequencies.

Future work entails the comprehensive analysis of all remaining devices, with particular emphasis on measuring their resonance frequency and the magnitude of charge generation.

Chapter 4

Characterization

The initial phase of the project involved conducting an analysis of the previous devices and selecting the most suitable ones for further analysis by the company. To determine the appropriate devices, an initial step involved microscopic observation to assess their condition. A significant number of devices were found to be heavily oxidized and damaged.

4.1 Measurement of Resonance Frequency and Membrane Thickness Determination

The next step involved measuring the resonance frequency using a Laser Doppler Vibrometer (LDV) station. The procedure included subjecting the device to sinusoidal acceleration through a piezoshaker, to which the device was attached. The piezoshaker, made of piezoelectric material, received an AC signal, while a laser from the LDV was directed towards the center of the device's membrane. Now, let us provide a brief explanation of this instrumentation.

The LDV operates on the principle of the Doppler effect. As the membrane vibrates, the reflected light from the laser is affected by the displacement, resulting in a change in the path of the reflected light. It contains an optical setup that enables an interference phenomenon between the incoming and reflected light. The change in optical path length over time is reflected as a frequency shift in the measurement beam, known as the Doppler frequency shift. This last one is directly proportional to the velocity of the sample. Consequently, an interference pattern is obtained. The collected signal is then processed using Fast Fourier Transform (FFT) to convert it from the time domain to the frequency domain. Additionally, the technique involves demodulation, which entails multiplying the signal with a sinusoid of a specific frequency.

Regarding the piezoshaker, it is actuated by a sinusoidal signal with a particular voltage amplitude and a frequency that sweeps from low frequencies up to hundreds of kHz. This allows for a comprehensive examination that includes the resonance frequency. This last one is identified by a significant peak in amplitude compared to the relatively flat part that characterizes lower frequencies. Moreover, the resonance curve exhibits a Lorentzian shape.

The following table presents the measured devices along with their respective resonance frequencies.

ID	Radius	$f_{R,experimental}$	$f_{R,simulation}$	t_{memb}
A1	1500 μm	80 kHz	100.94 kHz	60 μm
A2	1500 μm	60 kHz	100.94 kHz	60 μm
A3	1750 μm	54.7 kHz	74.88 kHz	60 μm
A4	1750 μm	50 kHz	74.88 kHz	60 μm
A5	1750 μm	60.8 kHz	74.88 kHz	60 μm
A6	2000 μm	52 kHz	57.73 kHz	60 μm
B1	2000 μm	24 kHz	12.33 kHz	20 μm*
C4	2250 μm	30.28 kHz	45.80 kHz	60 μm
C5	2250 μm	42 kHz	45.80 kHz	60 μm

Table 4.1: Data Table

Since the devices were not labeled, the thickness of the membrane in each accelerometer was unknown (except for the one marked with *). To address this, simulations were conducted for different membrane thicknesses: 20 μm, 60 μm, and 120 μm, as mentioned in the previous thesis. By utilizing the resonance frequency obtained from the measurements, the membrane thickness of each tested chip could be determined through the simulations.

Based on these obtained values, several conclusions can be drawn. Firstly, it is evident that the etching process for the membrane was not uniform, leading to variations in thickness. As observed in the previous thesis, the desired thickness was not achieved, with an average thickness of approximately 54 μm and an error of 8 μm (considering the case of 60 μm). This non-uniformity in membrane thickness can be attributed to factors such as inconsistent etching conditions or inadequate control over the etching process.

Furthermore, the measured resonance frequencies deviate from the simulated values. This discrepancy can be attributed to various factors, including degradation of the device itself due to factors like dust or contamination. These external factors can introduce additional damping or alter the mechanical properties of the device, leading to deviations in the resonance frequency.

These findings highlight the need for further investigation and optimization of the experimental setup to mitigate the aforementioned factors and improve the reliability and accuracy of the resonance frequency measurements.

4.2 Charge measurements

The next step in the experimental procedure involves conducting a charge measurement. Prior to this step, a resistance measurement was performed using a probe station to detect any short circuits. The resistance measurement entails applying a cyclic voltage signal ranging from 0V to 1V, then -1V, passing through 0V (to eliminate residual charges), and finally returning to -1V and back to 0V. By calculating the ratio between the voltage and the measured current, the resistance value can be determined. If the resistance falls within the range of $M\Omega$ to $G\Omega$, it indicates the absence of a short circuit. Conversely, if the resistance is low, such as in the case of device C5 where the resistance between the GND and OUTER electrode is 56.36 Ω, it suggests the presence of a short circuit. Consequently, this device should be excluded from further consideration.

After ensuring the proper functioning of the remaining devices, the subsequent step involves affixing them onto a printed circuit board (PCB) and performing wire bonding between it and the chip.

The PCB consists of a simple board and includes a final SMA[1] connection, as depicted in the accompanying figure (4.1).
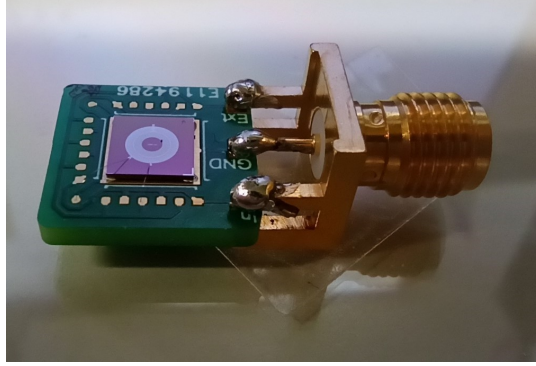

Figure 4.1: Picture of the PCB used. The chip is glued on top of the squared GND electrode.

The charge measurement was conducted on an optical bench, similar to the resonance frequency one. In this experimental setup, the chip was manipulated using a piezoshaker to induce motion, which was then measured using a laser Doppler vibrometer (LDV). An additional feature of this measurement is the simultaneous recording of the generated charges through the SMA connection. However, due to the expected minuscule charge values, the PCB was initially connected to a charge amplifier to amplify the signal and convert it into a measurable voltage.

Due to technical constraints, the laser Doppler vibrometer (LDV) measures velocity rather than acceleration directly. However, by multiplying the measured velocity by the frequency, the desired acceleration quantity can be obtained. This calculation is facilitated by the sinusoidal displacement signal sent to the piezoshaker is $z = A \cdot \sin(2\pi f t)$. The first time derivative of displacement yields velocity, expressed as $v = A \cdot (2\pi f) \cdot \cos(2\pi f t) = z \cdot (2\pi f)$. Finally, the second time derivative of displacement provides the acceleration as $a = -A \cdot (2\pi f)^2 \cdot \sin(2\pi f t) = -z \cdot (2\pi f)^2$. When the AlN piezoelectric layer operates correctly and the experimental setup is well optimized to minimize charge leakage, the voltage output signal from the device should precisely follow the input acceleration signal.

Furthermore, the ultimate goal of this study is to determine the device's responsivity, expressed in pC/g, which quantifies the amount of charge generated per unit of g-acceleration. To achieve this, the voltage output from the charge amplifier needs to be converted back into a charge signal knowing the two circuits implemented in the amplifiers.
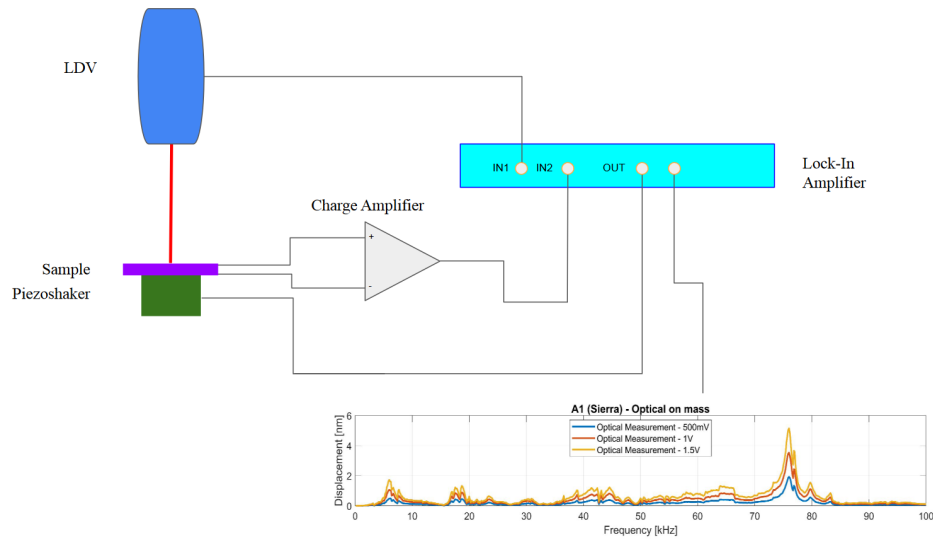
---

[1]SMA: SubMiniature version A

Figure 4.2: Scheme of the experimental setup for charge measurements

With these components in place, the next step is to calculate the responsivity. However, it is necessary to modify the acceleration and observe the resulting effect on the measured charge. Based on the aforementioned formulas, there are two approaches to increasing the acceleration:

- Increasing the amplitude: This was accomplished by applying three different voltage amplitudes (0.5V, 1V, and 1.5V) as input signals to the piezoshaker.

- Increasing the frequency: This can be achieved by sweeping the frequency of the input signal.

In the first case, the charge value at resonance was divided by the quality factor. Subsequently, the acceleration value at resonance was determined. The ratio between these two values represents the responsivity. As three different amplitudes were tested, it is crucial to ensure that the obtained responsivities are similar. Fitting these three data points yields a flat straight line.

In the second case, the experimental charge curve was directly divided by the corresponding acceleration curve. The average value obtained from this division was considered as the responsivity. The following summary table presents the selected devices for the company and their respective responsivities.

Sensor	Amplifier	Mode	Responsivity (pC/g)
A1	Sierra	Amplitude	0.0011
		Frequency	0.0052
	Tia	Amplitude	0.0276
		Frequency	0.0127
B1	Sierra	Amplitude	0.0021
		Frequency	0.0062
	Tia	Amplitude	0.0232
		Frequency	0.0188

Table 4.2: Responsivity Data - Lab measurements

Sensor	Responsivity (pC/g)
A1	0.0041
B1	0.0016

Table 4.3: Responsivity Data - Company measurements

Let us now discuss the results and identify the areas that can be improved for the fabrication of future devices. Firstly, it is observed that the responsivity values differ between the two modes of increasing acceleration. This discrepancy indicates a residual frequency dependence. Additionally, there is a substantial difference in the responsivity values obtained using the two amplifiers. Comparing our measured responsivities with the values provided by the company, it can be concluded that the Sierra amplifier outperforms the Tia[2] amplifier. The last one leads to an overestimation of responsivity, whereas the company-provided values align more closely with those obtained using the Sierra amplifier.

Taking into consideration the specified requirements provided by Meggitt and the results obtained from the characterization of the previous devices, we can establish a comprehensive schedule outlining our objectives for the next phase:

1. Working Frequency: The target is to operate within the frequency range of 20-30 kHz to ensure compatibility with the intended application.

2. Resonance Frequency: Aim to achieve a resonance frequency approximately 2-3 times higher than the working frequency, ideally around 90 kHz. This resonance behavior is crucial for optimal device performance.

3. Responsivity: The goal is to attain a responsivity of 0.5 pC/g. It is imperative to explore methods to maximize the amount of charge obtained to achieve higher responsivity values compared to the measured ones.

4. Fabrication: Emphasize the need for improved membrane uniformity during the fabrication process. Simplification of the fabrication techniques should be prioritized to mitigate potential issues and streamline the manufacturing process.

5. Characterization: Minimize potential leakage effects by utilizing smaller cables and selecting electrical components with low capacitance. This approach ensures precise and reliable characterization of the devices.

These requirements provide a foundation for the subsequent simulation phase, enabling the development of an optimized design and further refinement of the devices.

---

[2]TIA: Trans-Impedance Amplifier

Chapter 5

Simulations

5.1 COMSOL modelling

COMSOL is a multiphysics software that provides a user-friendly interface for creating and solving simulation models, while FEM is a numerical technique used to discretize physical domains and approximate solutions to differential equations.

The combination of COMSOL and FEM allows engineers and researchers to tackle a wide range of problems in various fields, including mechanical, electrical, thermal, and fluid dynamics. By dividing a physical domain into smaller elements, FEM discretizes the equations governing the system's behavior, enabling accurate numerical solutions.

These are fundamental tools for the project since it is needed to understand the behaviour of the vibrometer before proceeding with its design and fabrication. In particular, playing with all the geometrical parameters and the materials allows to find the best trade off condition between high resonance frequency and large amount of generated charges. As written in the last chapter the goal is to obtain an accelerometer with a resonance frequency around 90 kHz; given this constraint the goal is to obtain the largest generation of charge.

5.1.1 Model setup

Following the steps done in the previous works ([6, 5]), the accelerometer is modeled in COMSOL as a membrane with a proof mass. This is done by exploiting the *Axial symmetry 2D* functionality that allows the use of only 2 rectangles: a long and thin one for the membrane and a thick one for the seismic mass, as showed in the figure 5.1a. As one can understand from the name of this feature, by only using a 2D geometry it is possible to get a 3D device thanks to the rotation of the the 2D plane around the vertical axis positioned in the origin (0,0). This feature reduces the complexity of the mesh and so the computational time.

In order to model *Piezoelectricity* the COMSOL's *Multiphysics* tool has to be taken into account: *Electrostatics* in addition to *Solid mechanics*.
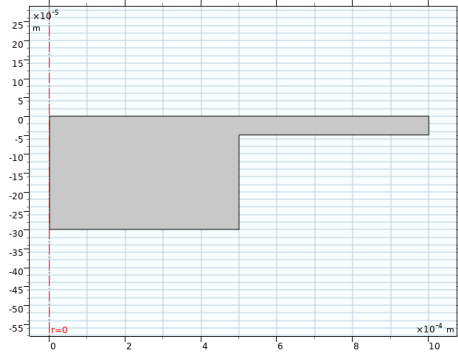
(a) 2D geometry
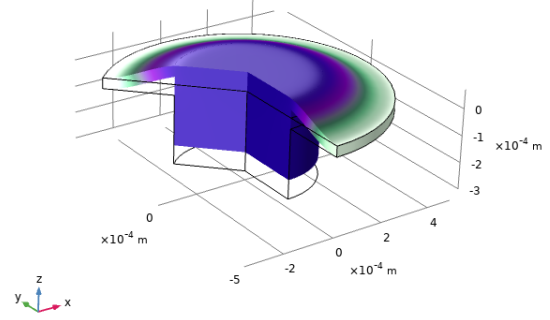
(b) 3D geometry

Figure 5.1: 2D and 3D geometries of the simulated accelerometer

5.1.2 Materials

The wafer that will be used for the fabrication is an SOI[1] wafer. It is composed by: 400 μm of Si (bottom), 3 μm buried oxide (SiO2), 75 μm of Si (top). The choice of using this type of wafer ensures to achieve the goal of a uniform Si membrane since it will be directly the top silicon layer; in this way we reduce also etching related issued. Anyway for the first simulations only Si is used for simplicity.

Whereas for the electrodes platinum (Pt) is used and finally the piezoelectric layer is aluminium nitrite (AlN).

Concerning this last material, all the piezoelectric parameters were taken from the previous work [6]:

$$e = \begin{bmatrix} 0 & 0 & 0 & 0 & -3.84 & 0 \\ 0 & 0 & 0 & -3.84 & 0 & 0 \\ -1.92 & -1.92 & 4.96 & 0 & 0 & 0 \end{bmatrix} \frac{pC}{N}$$

$$c = \begin{bmatrix} 410 & 149 & 99 & 0 & 0 & 0 \\ 149 & 410 & 149 & 0 & 0 & 0 \\ 99 & 149 & 410 & 0 & 0 & 0 \\ 0 & 0 & 0 & 125 & 0 & 0 \\ 0 & 0 & 0 & 0 & 125 & 0 \\ 0 & 0 & 0 & 0 & 0 & 125 \end{bmatrix} GPa$$

$$\epsilon = \begin{bmatrix} 9 & 0 & 0 \\ 0 & 9 & 0 \\ 0 & 0 & 9 \end{bmatrix} \times 8.854 \times 10^{-12} \frac{F}{m}$$

5.1.3 Solid mechanics

For what concerns the clamping part, in order to reduce the computational cost an additional rectangle is not used but only a *Fixed constraint*. This tool permits to fix the right end of the membrane simulating the silicon clamping.

Moreover also the *Gravity* tool is added to simulate *1g* of acceleration above the entire structure. In the next subsections the importance of this feature will be explained.

---

[1]Silicon - on - insulator

5.1.4 Electrostatics

After the selection of the piezoelectric layers, terminals are added: GND (ground - Bottom Pt layer), IN (Inner Pt layer) and OUT (Outer Pt layer). This is necessary for the stationary study for the calculation of the generated charges since all of them are collected by the Pt-electrodes.
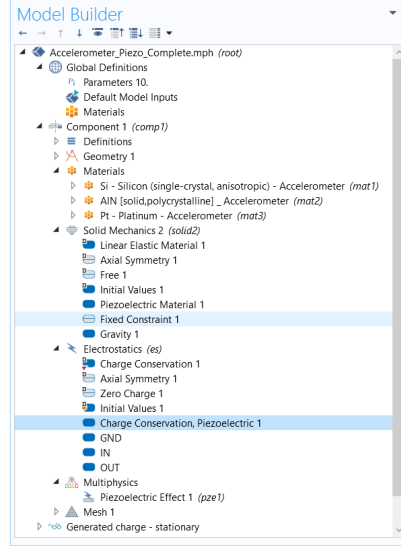
Figure 5.2: Model builder section in COMSOL

5.1.5 Mesh

Once the geometry of a model has been built and the boundary conditions defined, the subsequent stage in FEM involves meshing. Meshing entails dividing the model into nodes, with the number of nodes varying depending on the level of mesh refinement. Employing a highly refined mesh with a substantial number of nodes leads to a more precise solution, in contrast to a sparser mesh with only a few nodes. Nonetheless, increasing the mesh resolution results in longer computation times.

After conducting various simulations, it was determined that the optimal mesh configuration consists of rectangles that are distributed differently within the various domains. This is because the membrane and proof mass do not require a high level of discretization, while the piezoelectric material and the electrodes necessitats a greater number of nodes to accurately calculate the generated charge. To achieve this, a *User-controlled mesh* approach was employed. Additionally, the *Mapped* setting was implemented with different *Distributions*.

5.1.6 Generated charges - Stationary study

The *Stationary* study is used when field variables do not change over time, such as in stationary problems. In electromagnetics, it is used to compute static electric or magnetic fields, as well as direct currents. In heat transfer, it is used to compute the temperature field at thermal equilibrium. In solid mechanics, it is used to compute deformations, stresses, and strains at static equilibrium. In fluid flow, it is used to compute the steady flow and pressure fields. In chemical species transport, it is used to compute steady-state chemical composition in steady flows. In chemical reactions, it is used to compute the chemical composition at equilibrium of a reacting system.

As aforementioned one of the goals of this simulation is to calculate the amount of generated charges

and therefore the membrane as to be subjected to a motion, since the piezoelectric layer has to be under mechanical stress. Therefore the *gravity* tool (5.1.3) is necessary. In this way the membrane is displaced by 1-g acceleration. Thanks to the calculation of the displacement COMSOL can also evaluate the charge within IN and OUT terminals.

5.1.7 Resonance frequency - Prestressed,Eigenfrequency study

The Eigenfrequency Prestressed study is used to compute eigenfrequencies and eigenmodes that are influenced by a prior static load.

The study consists of two study steps: a *Stationary* study step followed by an *Eigenfrequency* study step. The study computes the eigenfrequencies and the shapes of the eigenmodes when influenced by a prior static load on the structure.

Moreover this study does not allow to keep the results of the stationary step and so it is not possible to obtain the charge within the terminals. In addition to this, the eigenfrequency study step calculate the mode shape of the membrane that cannot be treated as real displacement in the space. This represents the reason why two separate studies are needed.

Moreover it is used to evaluate only the first eigenfrequency that represents the resonance frequency of the device.

5.2 Simulation for enhanced charge generation

In light of the fixed membrane thickness of 75 μm, which was determined by the selection of the SOI wafer as mentioned earlier, a simulation was conducted to explore different mass thicknesses ranging from 75 μm up to 275 μm.
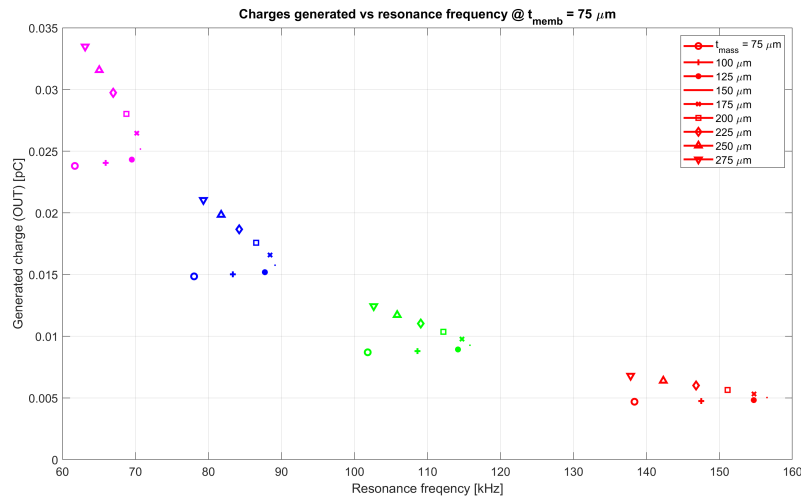
Figure 5.3: Simulation results (Red corresponds to 1500 μm, green 1750 μm, blue 2000 μm, magenta 2250 μm)

This investigation encompassed four distinct membrane radii: 1500 μm, 1750 μm, 2000 μm, and 2250 μm. The ratio between the membrane radius and the mass radius remained consistent at 0.5, as described in [6, 5]. Additionally, the electrode positions were left unaltered, with the IN and OUT electrodes placed solely on the half part of the membrane without the seismic mass. A hollow

section was positioned precisely at half of the distance from the beginning of IN electrode and the end of the OUT electrode. The ensuing results are summarized in the previous graph (Fig. 5.3). Based on the observed results, it is evident that the device without a proof mass exhibits comparable behavior to the device with a proof mass. This led us to explore the possibility of enhancing charge generation by altering the electrode positions, considering that the resonance frequencies meet the requirements outlined in the preceding section. To achieve this, we performed a simulation without electrodes. By obtaining the displacement profile of the membrane along its length, we calculated the second spatial derivative, representing the structural stress. Refer to the figure 5.4.

Our objective is to position the IN electrode where the second derivative is positive, while placing the OUT electrode where it is negative. This arrangement ensures that charge cancellation is avoided and a maximum number of generated charges are captured. Additionally, the hollow section should be positioned where the stress is zero.
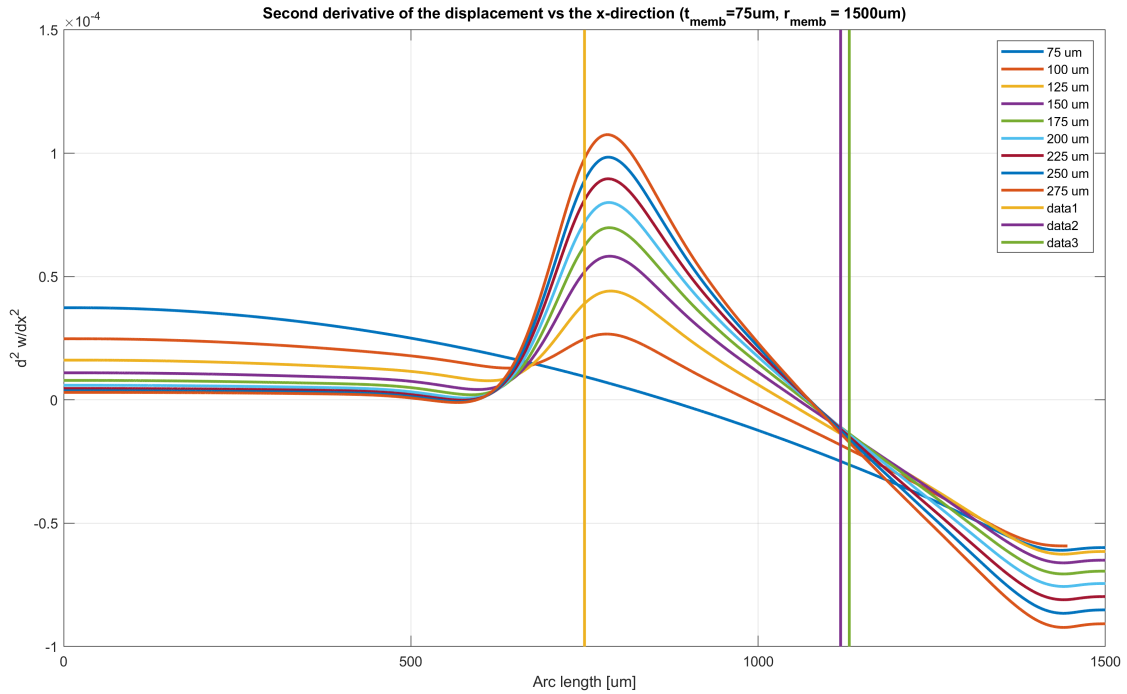
Figure 5.4: Second spatial derivative of the displacement along the length of the membrane for different mass thicknesses ($r_{memb} = 1500\mu m$); the 3 straight lines indicated the electrodes positioned following the old the design.

In the specific case of a mass thickness of 75 μm, i.e., without a proof mass, when the IN and OUT electrodes are positioned as described, we achieved an increase in charge generation of approximately 40%. This outcome aligns precisely with the goals set for the new devices. The absence of a seismic mass not only reduces fabrication complexities by eliminating photolithographic and etching steps but also allowed a large membrane uniformity. The figures (5.5a,5.5b) below show the final geometries at the end of the aforementioned simulation.
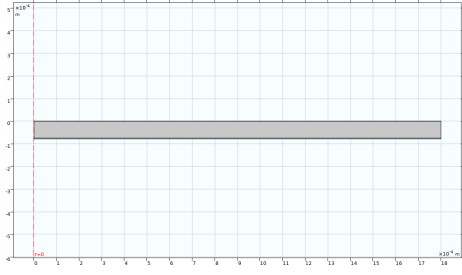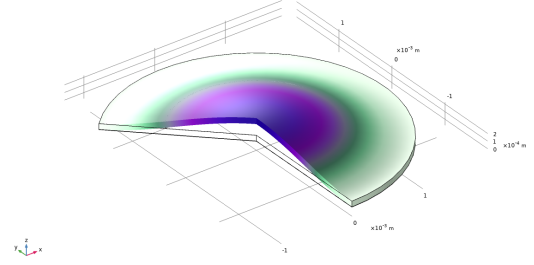
(a) 2D geometry   (b) 3D geometry

Figure 5.5: 2D and 3D geometries of the accelerometer without the proof mass with improved performance.

5.3   Future challenges

It is important to introduce a potential limitation. One aspect that has yet to be fully considered is the potential motion of the clamping mechanism itself. While the membrane undergoes vibrations, there is a possibility that the external part of the device may also experience displacement.

To assess the impact of this lateral unwanted motion on the overall generation of charge, further simulations will be conducted. The goal is to determine whether the charge generated by the lateral displacement is significant in comparison to the charge generated by the vertical motion of the membrane. If the ratio between these two types of charge generation remains sufficiently small, it would be feasible to proceed with the fabrication of the device. However, if the lateral displacement significantly affects the total charge generated, alternative solutions will need to be explored.

One potential solution to mitigate this issue could involve increasing the size of the chip itself. By doing so, the mass of the clamped parts would be increased, potentially reducing the impact of lateral displacement and its effect on charge generation.

Chapter 6

Microfabrication

The immediate objective is to develop the design for an enhanced and improved device. Leveraging the capabilities of the new device, we can establish the process flow and devise the mask design for the photolithographic steps.

To begin, let us summarize the previous decisions based on the prior characterization and simulation results. It was determined that the membrane thickness should be set at 75 μm, with no proof mass. Additionally, the position of the electrodes was adjusted to maximize charge generation in accordance with the stress curve.

Remaining unchanged are the material choice for the electrodes, which is Pt, and their thickness of 50 nm.

6.1 Electrodes and insulating layer

The initial challenge is to minimize charge leakage between the ground (GND) electrode and the top silicon (Si) layer of the wafer,since it is highly conductive.

Furthermore, for the deposition of the bottom electrode Pt, it is necessary to first apply a thin seed layer of AlN, specifically 25 nm thick. This layer serves as an initial isolation, but its primary purpose is to provide guidance for the crystallographic orientation.

Consequently, an additional layer, referred to as the *insulating layer*, needs to be introduced. There are two potential options for this layer:

1. Adding a SiO_2 layer.

2. Increasing the thickness of the AlN seed layer.

In order to determine the optimal solution, calculations were performed, with the objective of minimizing the ratios C_IN_PAD/C_IN and C_OUT_PAD/C_OUT. Let's describe these capacitances:

- C_IN and C_OUT represent the capacitances of the inner and outer electrodes, respectively. Their values depend on the thickness of the active AlN layer.

- C_IN_PAD represents the series capacitance of the IN electrode's pad, which is influenced by the thicknesses of both the seed and active layers, and the one of the GND pad, which is affected by the thickness of the insulating layer.

- C_OUT_PAD represents the series capacitance of the OUT electrode's pad and the GND electrode's pad.

The primary objective is to minimize the specified ratios. In terms of the physical aspect, this entails ensuring the preservation of all generated charges in the IN and OUT electrodes, while also minimizing potential charge leakage caused by the presence of the IN_PAD, OUT_PAD, and GND_PAD. To achieve this objective, three parameters need to be adjusted: the thickness of the active AlN layer, the thickness of the insulating layer, and the choice of the dielectric material, so a different permittivity constant (e.g., 3.9 for SiO_2 and 9.2 for AlN).

To begin the investigation, the height of the AlN layer sandwiched between the Pt electrodes was fixed at 200 nm. With this configuration, calculations were conducted to determine the ratios. The graph presented below (Fig. 6.1) specifically depicts the ratio C_IN_PAD/C_IN for various dielectric thicknesses. The red dots represent the scenario where only the seed layer is utilized, while the blue dots represent the scenario where SiO_2 is used as the insulating layer (with a 25 nm of AlN seed layer always employed for crystallographic orientation).
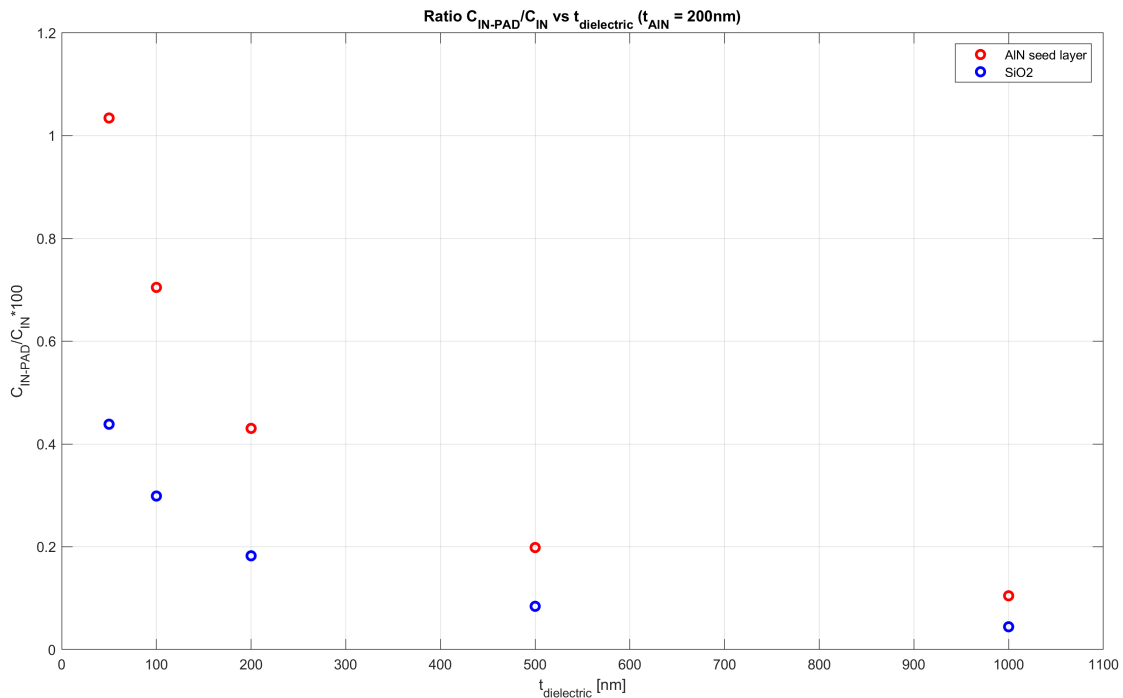
Figure 6.1: Ratio of C_IN_PAD to C_IN for Different Dielectric Thicknesses

Based on the analysis of this graph, it can be concluded that SiO_2 is the most favorable choice. When considering equal thicknesses, the ratio is significantly smaller compared to using AlN. As a result, for the initial fabrication, an insulating layer thickness of 200 nm has been decided upon.

6.2 New design

We are now prepared to outline the various fabrication steps that will form part of the process flow, taking into account the device's specific parameters. It should be noted that the number of steps is reduced compared to the previous design, as there is no longer a proof mass included. Additionally, based on ongoing work within the EPFL's cleanroom, we have made the decision to eliminate the parylene coating step, as it has proven problematic during the removal process, often

resulting in undesired release. Consequently, the design for the lithographic step has been updated using Clewin5 and is depicted in the figure below.
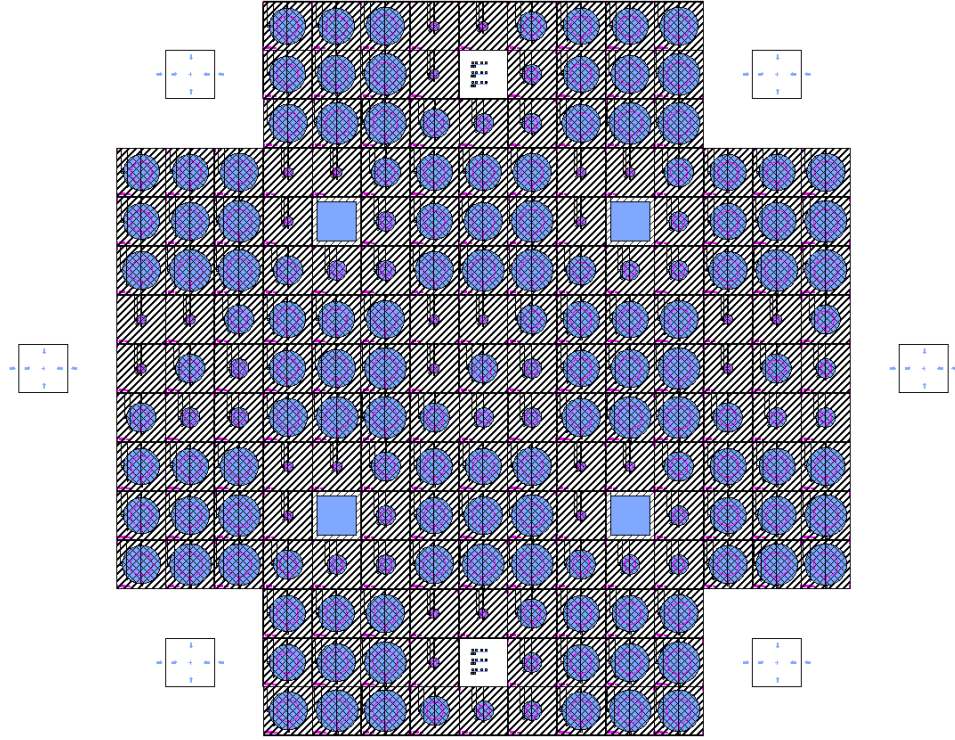
Figure 6.2: Design of the mask for all the photolithographic steps

Upon reviewing the revised process flow (A), it becomes evident that there are four distinct steps related to photolithography. As depicted in the aforementioned figure, each step corresponds to a different layer. The first layer is responsible for defining the ground (GND) electrode, followed by a layer for the inner (IN) and outer (OUT) electrodes. The third layer serves the purpose of creating an aperture through which the GND pad can be accessed since this area will be previously covered by AlN. Lastly, the final layer is dedicated to the backside processes required for releasing the membrane.

It is important to note that the fabrication process has not yet commenced, and therefore all the results, issues, and updates will be documented and presented in a future report.

Chapter 7

Conclusions

In conclusion, this thesis project aimed to develop a vibrometer for Meggitt, focusing on the design and simulation of a new accelerometer with improved performance characteristics. Through a comprehensive characterization of previous devices and simulations based on new constraints, we have made significant findings. The key discovery is the elimination of the seismic mass and the optimization of electrode geometry to enhance charge generation and responsivity.

Building upon these findings, a process flow for the fabrication of the new accelerometer has been outlined. The forthcoming phase will involve the realization of the device using the new design, which is anticipated to face challenges during the cleanroom processes. However, we are confident that by tackling these obstacles systematically, we will overcome them and proceed towards successful fabrication.

While the absence of a proof mass in this accelerometer simplifies fabrication, it does result in reduced charge generation. Thus, achieving an optimal trade-off between resonance frequency and charge generation remains a critical consideration.

Looking to the future, the next steps involve characterizing the new devices and evaluating their performance against the desired requirements. If the results meet the established criteria, the focus will shift towards designing and fabricating the packaging for the accelerometer, ultimately leading to the integration of the final product into relevant systems such as aircraft gearboxes.

In terms of performance improvement, the adoption of a doped piezoelectric material, specifically AlScN, holds promise due to its significantly larger piezoelectric coefficient. However, the deposition process for this material presents additional challenges that need to be addressed.

Overall, this thesis project has laid the foundation for the development of an advanced vibrometer, showcasing the potential of the new accelerometer design. By addressing limitations, characterizing the devices, and exploring material enhancements, we aim to contribute to the field of vibration measurement and offer valuable insights for industrial applications.

Bibliography
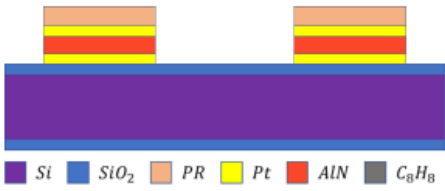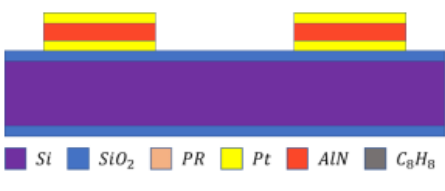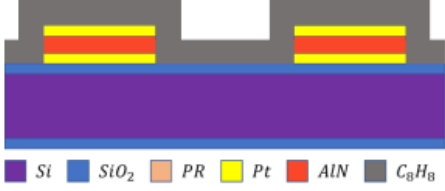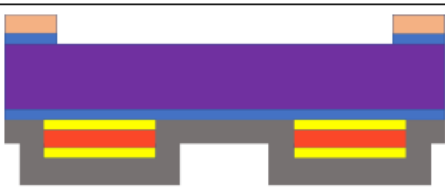
[1] Meggitt accelerometers:https://www.meggitt.com/products-services/accelerometers/.

[2] T Gordon Brown. Harsh military environments and microelectromechanical (mems) devices. In *SENSORS, 2003 IEEE*, volume 2, pages 753–760. IEEE, 2003.

[3] Renato Caliò, Udaya Bhaskar Rongala, Domenico Camboni, Mario Milazzo, Cesare Stefanini, Gianluca De Petris, and Calogero Maria Oddo. Piezoelectric energy harvesting solutions. *Sensors*, 14(3):4755–4790, 2014.

[4] Matthew W Hooker. Properties of pzt-based piezoelectric ceramics between-150 and 250 c. Technical report, 1998.

[5] Myriam Käppeli. Fabrication and characterization of mems piezoelectric accelerometers. Technical report, 2020.

[6] Bradley Petkus. Mems piezoelectric accelerometer for vibration sensing in harsh environments. Technical report, 2019.

[7] Stefan Johann Rupitsch. Piezoelectric sensors and actuators: Fundamentals and applications. 2021.

[8] Silvan Schmid, Luis Guillermo Villanueva, and Michael Lee Roukes. *Fundamentals of nanomechanical resonators*, volume 49. Springer, 2016.

[9] SAKM Tadigadapa and K Mateti. Piezoelectric mems sensors: state-of-the-art and perspectives. *Measurement Science and technology*, 20(9):092001, 2009.

[10] Mohammad Tahmasebipour and Ali Vafaie. A highly sensitive three axis piezoelectric microaccelerometer for high bandwidth applications. *Micro and Nanosystems*, 9(2):111–120, 2017.

[11] Bahareh Yaghootkar, Soheil Azimi, and Behraad Bahreyni. A high-performance piezoelectric vibration sensor. *IEEE Sensors Journal*, 17(13):4005–4012, 2017.
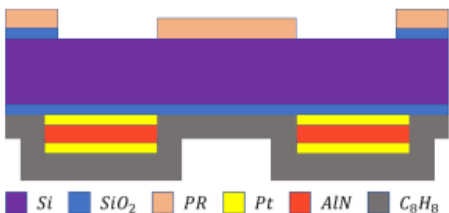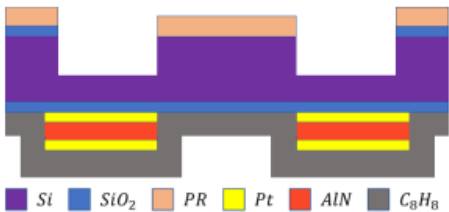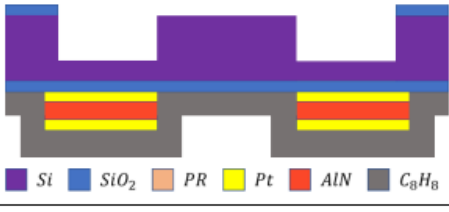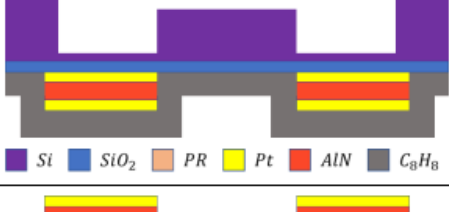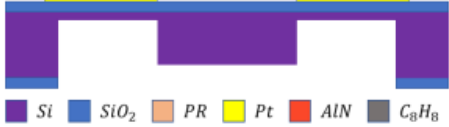
Appendix A

Previous process flow

Step-by-step process outline
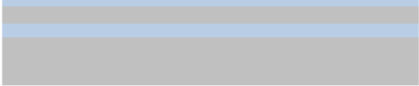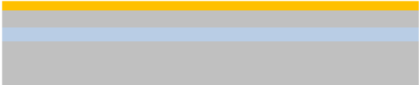
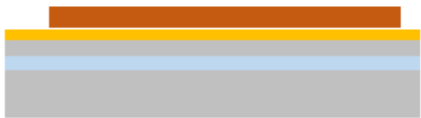| Step	Process description	Cross-section after process
00	**Start:** 500 nm oxide (SiO₂), 380 μm handle layer (Si)	
01	*Frontside* **Photolithography 1ˢᵗ layer** Machine: *EVG 150 + MLA 150* PR : *0.4 μm LOR A5 + 1.1μm AZ1512*	
02	*Frontside* **Sputtering:** *Seed layer (AlN) + 50 nm Pt* Machine: *Spider 600 + Plade «Solvent» Z1 Wet Bench LOR*	
03	*Frontside* **Lift-off** Equipment: *Plade «Solvent» Z1 Wet Bench LOR*	
04	*Frontside* **Sputtering:** *100 nm AlN + 50 nm Pt* Machine: *Spider 600*	
05	*Frontside* **Photolithography 2ⁿᵈ layer** Machine: *ACS 200 + MLA 150* PR : *AZ ECI 3007 − 1.5 μm*	

06	*Frontside* **Plasma etching:** *50 nm Pt + 100 nm AlN* Machine: *STS Multiplex ICP*	 ■ *Si* ■ *SiO₂* ■ *PR* ■ *Pt* ■ *AlN* ■ *C₈H₈*
07	*Frontside* **Resist stripping** Equipment: *Tepla GiGAbatch (60s resist strip high), Remover 1165 UFT wetbench Z2*	 ■ *Si* ■ *SiO₂* ■ *PR* ■ *Pt* ■ *AlN* ■ *C₈H₈*
08	*Frontside* **Evaporation deposition:** *5+ μm parylene*	 ■ *Si* ■ *SiO₂* ■ *PR* ■ *Pt* ■ *AlN* ■ *C₈H₈*
09	*Backside* **Photolithography 3rd layer** Machine: *EVG 150 + MLA 150* PR: *1.5 μm AZ 1512*	 ■ *Si* ■ *SiO₂* ■ *PR* ■ *Pt* ■ *AlN* ■ *C₈H₈*
10	*Backside* **Plasma etching:** *500 nm SiO2* Machine: *SPTS APS*	 ■ *Si* ■ *SiO₂* ■ *PR* ■ *Pt* ■ *AlN* ■ *C₈H₈*
11	*Backside* **Resist stripping** Equipment: *Remover 1165 UFT wetbench Z2*	 ■ *Si* ■ *SiO₂* ■ *PR* ■ *Pt* ■ *AlN* ■ *C₈H₈*

12	*Backside* **Photolithography 4th layer** Machine: *EVG 150 + MLA 150* PR: *5 μm AZ 9260*	 Si SiO₂ PR Pt AlN C₈H₈
13	*Backside* **Plasma etching:** *260 - 370 μm Si* Machine: *AMS 200*	 Si SiO₂ PR Pt AlN C₈H₈
14	*Backside* **Resist stripping** Equipment: *Remover 1165 UFT wetbench Z2*	 Si SiO₂ PR Pt AlN C₈H₈
15	*Backside* **Plasma etching:** *80 μm Si* Machine: *AMS 200*	 Si SiO₂ PR Pt AlN C₈H₈
16	*Frontside* **Plasma etching:** *5+ μm parylene* Machine: *Tepla GiGAbatch*	 Si SiO₂ PR Pt AlN C₈H₈

Appendix A

Current process flow

Step	Process description	Cross-section after process
00	**Start**: SOI wafer, 75 µm device layer (Si), 3 µm oxide layer (SiO_2), 400 µm handle layer (Si)	Si ▢ SiO_2 ▢ PR ▢ Pt ▢ AlN ▢ Al
01	**Dry Oxidation** CMi service 200nm SiO_2	Si ▢ SiO_2 ▢ PR ▢ Pt ▢ AlN ▢ Al
02	*Frontside* **Sputtering:** Seed layer 25 nm (AlN) + 50 nm Pt Machine: Spider 600	Si ▢ SiO_2 ▢ PR ▢ Pt ▢ AlN ▢ Al
03	*Frontside* **Photolithography 1st layer: Coating** Machine : ACS 200 PR: 1 µm AZ10XT-07 Automatic machine	Si ▢ SiO_2 ▢ PR ▢ Pt ▢ AlN ▢ Al
03	*Frontside* **Photolithography 1st layer: Exposure** Machine : MLA 150 (GDS file for the design) Dose > 95 (120) Defocus -1	Si ▢ SiO_2 ▢ PR ▢ Pt ▢ AlN ▢ Al

03	*Frontside* **Photolithography 1st layer: Development** Machine : ACS 200 PR: 1 µm AZ10XT-07 2x 1um recipe + SDR Z1 Plade Solvent (wash and clean the wafer) + Check on microscope Z1	▇ Si ▇ SiO$_2$ ▇ PR ▇ Pt ▇ AlN ▇ Al
04	*Front side* **Reflow:** 125° , 2 min, Z1 hotplate	▇ Si ▇ SiO$_2$ ▇ PR ▇ Pt ▇ AlN ▇ Al
05	*Front side* **Descum** Machine: Z2 – Tepla 1min O2 plasma (low power)	▇ Si ▇ SiO$_2$ ▇ PR ▇ Pt ▇ AlN ▇ Al
06	*Front side* **Ion Beam Etching:** 50 nm Pt Machine: IBE350 Medium_IBE (-10° + -70°) + Check on microscope Z1	▇ Si ▇ SiO$_2$ ▇ PR ▇ Pt ▇ AlN ▇ Al

07	*Front side* **Photoresist strip** Machine: 1' Tepla-HighPower + UFT Remover 1165 bath + 3' Tepla-LowPower	 Si ▪ SiO₂ ▪ PR ▪ Pt ▪ AlN ▪ Al
08	*Frontside* **Sputtering:** 200 nm AlN + 50 nm Pt SPIDER600	 Si ▪ SiO₂ ▪ PR ▪ Pt ▪ AlN ▪ Al
09	*Frontside* **Photolithography 2nd layer** Machine : ACS 200 + MLA 150 PR: AZ10XT-07 1.5 μm	 Si ▪ SiO₂ ▪ PR ▪ Pt ▪ AlN ▪ Al
10	**Reflow:** 125° , 2 min, Z1 hotplate	 Si ▪ SiO₂ ▪ PR ▪ Pt ▪ AlN ▪ Al
11	*Frontside* **Ion Beam Etching:** 50 nm Pt Machine: IBE350	 Si ▪ SiO₂ ▪ PR ▪ Pt ▪ AlN ▪ Al

12	*Frontside* **Resist stripping:** Machine: Tepla GiGabatch (60s resist strip high), Remover 1165 UFT wetbench Z2	 ■ Si ■ SiO$_2$ ■ PR ■ Pt ■ AlN ■ Al
13	*Frontside* **Photolithography (Access to pads):** Machine : ACS 200 (EVG 150) + MLA 150 PR: LOR 0.7 μm + AZ1512 1.1 μm	 ■ Si ■ SiO$_2$ ■ PR ■ Pt ■ AlN ■ Al
14	*Frontside* **Developper for longer time** 100 nm AlN Machine: Z13 Developer bench AZ726MIF – 1min	 ■ Si ■ SiO$_2$ ■ PR ■ Pt ■ AlN ■ Al
15	*Front side* **Descum** Machine: Z2 – Tepla 10s O2 plasma (low power)	
16	*Frontside* **Deposition (Evaporation):** Material : 500 nm Cr-Al Machine : EVA 760 – Z11	 ■ Si ■ SiO$_2$ ■ PR ■ Pt ■ AlN ■ Al

17	*Frontside* **Lift off** Machine: Z1 – Plade solvent	 ■ Si ■ SiO₂ ■ PR ■ Pt ■ AlN ■ Al
18	*Backside* **Photolithography (Membrane)** Machine : EVG + MLA 150 PR: *AZ 10XT-60 8µm*	 ■ Si ■ SiO₂ ■ PR ■ Pt ■ AlN ■ Al
19	*Backside* **Hard baking** *85degC > 8hours* *Z11 oven*	 ■ Si ■ SiO₂ ■ PR ■ Pt ■ AlN ■ Al
20	*Backside* **Plasma etching:** 400 µm Si Machine: SPTS Rapier	 ■ Si ■ SiO₂ ■ PR ■ Pt ■ AlN ■ Al
21	*Back side* **Resist stripping:** Machine: Tepla GiGabatch (60s resist strip high), Remover 1165 UFT wetbench Z2	 ■ Si ■ SiO₂ ■ PR ■ Pt ■ AlN ■ Al

| 22 | *Inspection*

Machine: Z1 SEM Zeiss Leo | |